(BL8B1)

Pd 3*p* core level x-ray absorption spectroscopy of ordered Pd_3Fe

Takayuki MURO, Shin IMADA, Ki-Seok AN, Ran-Ju JUNG,
Takeshi KANOMATA[A], and Shigemasa SUGA

Department of Material Physics, Osaka University,
Toyonaka, Osaka 560-8531
[A]Department of Applied Physics, Faculty of Engineering, Tohoku Gakuin University,
Tagajo, Miyagi 985-8537

Series of Pd-Fe alloys have been extensively studied as typical transition metal alloys showing several interesting properties. One of the characteristic properties of Pd-Fe alloys is the large local magnetic moments on the Fe sites, especially in the Pd-rich region, up to 3 μ_B in comparison with 2.2 μ_B in Fe metal. Although Pd metal is not ferromagnetic, very small amount of Fe makes it ferromagnetic and the dilute PdFe shows so-called giant-moment as large as 12 μ_B per impurity [1].

The previously observed x-ray absorption (XAS) spectrum in the Pd 3*p* core region of Pd_3Fe showed anomalously large structures in the photon-energy (hν) regions of about 7.5 eV higher than the $3p_{3/2}$ and $3p_{1/2}$ main peaks. Similar structures were also seen in the Pd 3*p* XAS spectra of Ni-Pd alloys [2]. One possibility for the origin of the separations between the main peaks and the higher-energy structures is that the main peaks stem from excitonic states in the XAS final state. The binding energies (E_B) of the $3p_{3/2}$ and $3p_{1/2}$ levels were obtained as 532.3 and 560.1 eV, respectively, from the XPS measurement. If the hν at the $3p_{3/2}$ and $3p_{1/2}$ main peaks of the XAS spectrum are smaller than the E_B of the $3p_{3/2}$ and $3p_{1/2}$ levels, the XAS main peaks might be the excitonic states. Unfortunately, the photon energy of the previously observed Pd 3*p* XAS spectrum had not been corrected by any other references.

We have measured the Pd 3*p* XAS spectrum of Pd_3Fe again and corrected the hν by the O 1*s* absorption at the BL8B1. The corrected hν at the Pd $3p_{3/2}$ and $3p_{1/2}$ main peaks of the XAS spectrum are 535.0 and 563.0 eV, which are larger than the E_B of the Pd $3p_{3/2}$ and $3p_{1/2}$ core levels, respectively. Therefore, we conclude that the separations between the main peaks and the higher-energy structures are not due to the exciton effect.

References

[1] J. Crangle and W. R. Scott, J. Apple. Phys. **36**, 921 (1965).
[2] S. Y. Park, S. Muto, A. Kimura, S. Imada, Y. Kagoshima, T. Miyahara, T. Hatano, T. Hanyu and I. Shiozaki, J. Phys. Soc. Jpn. **64**, 934 (1995).

(BL8B1)

Photodissociation of ozone in the *K* edge region

Tatsuo GEJO, Kazumasa OKADA[A], Toshio IBUKI[B] and Norio SAITO[C]

Institute for Molecular Science, Myodaiji, Okazaki 444-8585, Japan

[A]Department of Chemistry, Hiroshima Univ., Higashi-Hirosima 739, Japan

[B]Kyoto Univ. of Education, Fukakusa, Fushimi-ku, Kyoto 612, Japan

[C]Electro technical Laboratory, Umezono, Tsukuba-shi, 305-0045, Japan

The inner-shell excitation of different atoms in a molecule leads to significant different photodissociation pathway. This effect is called site-specific dependence of fragmentation and has been observed in the *K* edge excitations of N_2O, CF_3CH_3 , CF_2CH_2, BF_3 and OCS. In view of this, it is of interest to investigate the dissociation of ozone in the *K* shell excited state. We have previously observed two distinct peaks around 529 and 536 eV in the ion yield spectra of ozone [1]. The first peak at 529 eV has been assigned as the $\pi^*(2b_1)\leftarrow O_T(1s)$ resonance transition of the terminal oxygen atom and the second around 536 eV as the excitation to the π^* level from the center O(1s) [1]. However, the latter has a wide bandwidth. Performing the molecular orbital (MO) calculations based on the SCF approximation, this band has been deconvoluted by two components: The calculation shows that one is the $\pi^*(2b_1)\leftarrow O_C(1s)$ transition, as we expected, and another is $\sigma^*(7a_1)\leftarrow O_T(1s)$ transition [1], where the O_C and O_T mean the terminal and center oxygen atoms, respectively. The excitation from these different 1s levels of ozone is expected to give different photodissociation or ionization pathway.

The time-of-flight (TOF) spectra measurement is a useful tool for investigating the pathway of ionic fragmentation of a molecule. In addition to this, angle-resolved measurement using the TOF apparatus provides information about electronic state of the decomposing molecule: The dipole transition probability depends on the molecular orientation with respect to the electric vector of polarized light. The *KVV* Auger decay or autoionization occurs within 10^{-14} s in the *K* shell excited molecule, while the rotational period of molecule is longer than 10^{-13} s. Hence the initial memory of the innermost core excited molecule may not be faded in fragmentation.

The TOF mass spectra were measured at 529.0, 535.7, and 544.6 eV for the $\pi^*(2b_1)\leftarrow O_T(1s)$, $\pi^*(2b_1)\leftarrow O_C(1s)/\sigma^*(7a_1)\leftarrow O_T(1s)$, and $\sigma^*\leftarrow O_C(1s)$ transitions, respectively. The detector axis was set at 0 degree (denoted as "horizontal") or 90 degrees (denoted as "vertical") with respect to the linearly polarized synchrotron radiation. Fig. 1 shows the TOF spectra at the vertical and horizontal positions excited at 529.0, 535.7 and 544.6 eV. In these spectra, the contribution from O_2 was subtracted. At the excitation energy 529.0 eV, the O^+ ion ejected to the vertical direction consists of three peaks with local maxima: The center one is presumably due to O^+ and O_2^{2+} with no kinetic energy. Two wing peaks should be O^+ fragments. On the other hand, the energy distribution obtained from the ions at the horizontal position shows the relatively narrow single O^+ peak. The difference of these two shapes arises from the fact that the O^+ fragment is preferably emitted to the vertical direction with some kinetic energy. Since the geometry of ozone in the ground state is bent (C_{2v}), this is consistent with our previous assignment that the 529 eV band is the $\pi^*(2b_1)\leftarrow 1s(2a_1)$ transition, whose transition moment lies perpendicular to the C_{2v} molecular plane. In contrast to this, at an excitation energy of 535.7 eV, the O^+ ion ejected both to the vertical and to the horizontal direction consists of three peaks. This implies that the O^+ fragment ions were ejected more isotropically.

Table 1 shows the appearance of fragments O_3^+, O_2^+ and O^+ and O^{2+} depending on the excitation energies. The main products observed were O_2^+ and O^+. Those fragments account for 85-90 % of products for these excitation energies. The parent O_3^+ was also produced. However, it is less than 8 % of total ions. In table 1 the fragment distributions are similar in the excitations of center O(1s) electrons at 535.7 and 544.6 eV, which means the effect of excitation energy on the fragmentation is not considerable. On the contrary, the O_2^+ fragment is preferably formed at the $\pi^*(2b_1)\leftarrow O_T(1s)$ excitation, especially 42% at the horizontal experiment. This enhancement of O_2^+ can be attributed to the atomic site selectivity of the relaxation processes following the initial excitation. That is, the core hole associated with the terminal oxygen produces the large yield of molecular O_2^+ fragment ion.

[1] T. Gejo, K. Okada and T. Ibuki, *Chem. Phys. Letters* 277 (1997) 497.

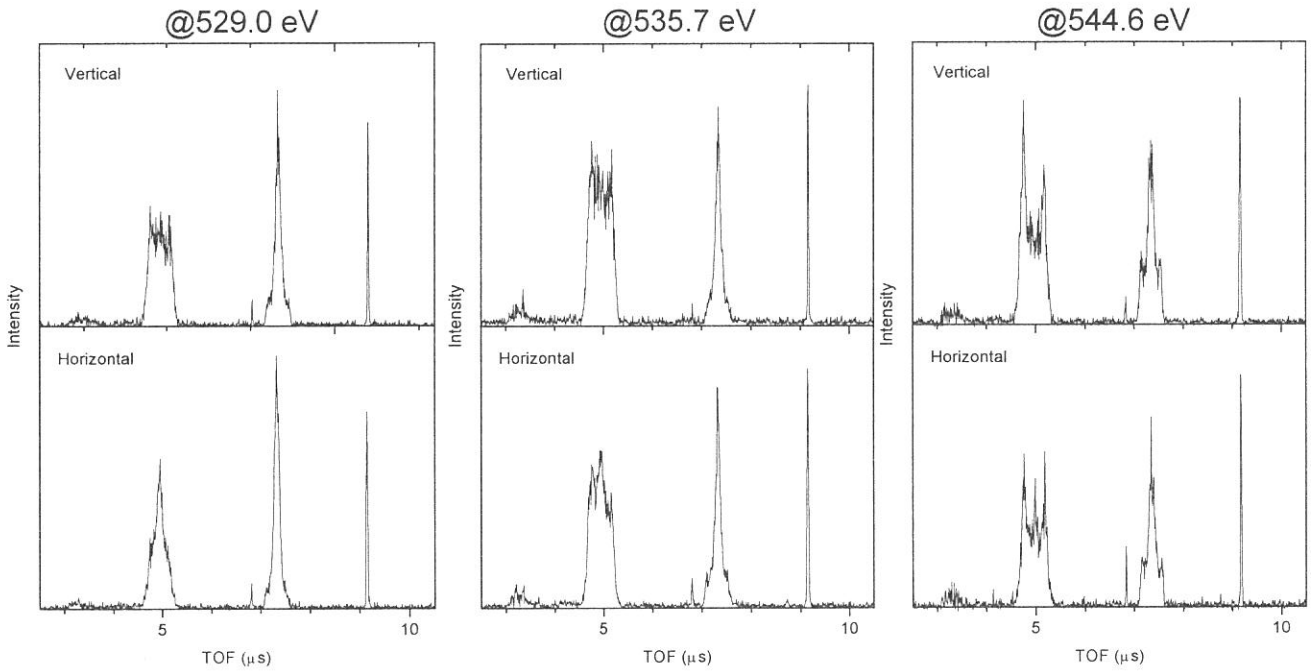

Fig. 1: TOF spectra obtainedwhen the detector is set to the horizontal and vertical to the direction of polarization of light.

Table 1: The branching ratios of ion photofragments observed at three energies.

	529.0eV (%)	535.7eV (%)	544.6eV (%)
O_3^+	8(//) 6(⊥)	8 5	8 7
O_2^+	42 37	30 25	32 33
O^+	46 54	58 63	55 54
O^{2+}	4 5	5 6	5 5

Left values were measured when the polarization is set to horizontal position (//) while right ones were measured when it is set to vertical position (⊥).

(BL 8B1)

Characterization of the Catalysts for the Oxidative Cracking of n-Butane by O K-edge XANES

Sakae TAKENAKA*, Shoji KOBAYASHI*, Tomoko YOSHIDA**, Ichiro YAMANAKA*, and Kiyoshi OTSUKA*

*Faculty of Engineering, Tokyo Institute of Technology, Meguro, Tokyo, 152-8552
**Center for Integrated Research in Science and Engineering, Nagoya University, Nagoya, 464-8603

1. Introduction

A promising area of light alkanes utilization is the conversion to unsaturated hydrocarbons. We have found that rare-earth metal oxide catalysts are effective for the oxidative cracking of n-butane to form ethene and propene. Furthermore, the addition of Li^+ ions to rare-earth metal oxide catalysts caused suppression of total oxidation of n-butane and increase in olefin yields. The addition of Li^+ ions to rare-earth metal oxides would bring about the change of chemical property of the lattice oxygen in Y_2O_3. In this study, we investigated the structural change of Y_2O_3 by the addition of Li^+ ions using O K-edge XANES spectroscopy and XRD, in order to obtain the information about active species for the oxidative cracking of n-butane.

2. Experimental

The Li^+-added Y_2O_3 was prepared by impregnating Y_2O_3 with an aqueous solution of Li_2CO_3, following by calcination at 1073 K under an air stream. The experiment for the oxidative cracking of n-butane was carried out using a conventional gas flowing system. The O K-edge XANES spectra of catalysts were recorded at room temperature in a total electron yield mode at BL-8B1 at UVSOR. In most measurements, the G2 grating and entrance and exit slits both of 20 μm width were utilized. The sample was put on a Cu-Be dinode which is attached to the first position of the electron multiplier.

3. Results and Discussion

Fig. 1 shows the changes of n-butane conversion and olefin yield by the added amounts of Li^+ ions in the oxidative cracking of n-butane over Li^+-added Y_2O_3 catalysts at 1023 K. The addition of Li^+ ions to Y_2O_3 catalysts resulted in the decrease of the n-butane conversion, however, the total oxidation suppressed and the olefin yields increased by the addition of Li^+ ions. This result indicates that the addition of Li^+ ions to Y_2O_3 brings about the formation of active sites on Y_2O_3 for the selective oxidation of n-butane to olefins.

Fig. 2 shows XRD patterns of Y_2O_3 and Li^+-added Y_2O_3 samples. The XRD pattern of Y_2O_3 was identical to that Li^+-added Y_2O_3. This result suggests that new phase was not formed by the addition of Li_2CO_3 to Y_2O_3.

Fig.3 shows O K-edge XANES spectra of Y_2O_3 and Li^+-added Y_2O_3 catalysts. In the XANES spectrum of Y_2O_3, two peaks were observed at ca. 534 and 538 eV. The first peak is assigned to the transition from O 1s to the hybridized orbital of the oxygen 2p and yttrium 4d (t_{2g}), and the other to e_g. By the addition of Li_2CO_3 to Y_2O_3, the feature of the XANES spectra changed. As the amounts of added Li_2CO_3 increased, the XANES spectra of Li^+-added Y_2O_3 got similar to that of Li_2CO_3. The XANES spectrum of Li^+(10 wt% as Li_2O)-added Y_2O_3 was identical with that of Li_2CO_3. This result indicates that Li^+-added Y_2O_3 was covered with Li_2CO_3 gradually, as the amounts of Li+ ions increased. In the XRD profile of Li^+-added Y_2O_3 catalyst, no peak due to Li_2CO_3 was found. Hence, Li_2CO_3 would be present on Y_2O_3 surface as thin layers. In Fig. 1, it is found that by the addition of Li^+ ions, the conversion of n-butane became lower and the selectivities to ethene and propene became higher. Therefore, the catalysts covered with Li_2CO_3 are effective for the formation of olefins.

Li^+-added Y_2O_3 was calcined at 1073 K, when the catalyst was prepared. During the calcination, CO_3^{2-} from Li_2CO_3 would be decomposed. Li_2CO_3 on the catalysts, which was

observed in the XANES spectra of Li^+-added Y_2O_3, may be formed during the preservation in the air after the preparation. Because Li^+-added Y_2O_3 catalyst has a strong basic property, CO_2 in the air was adsorbed on the catalyst to form Li_2CO_3.

Li^+-added rare-earth metal oxide catalysts are also effective for the oxidative coupling of methane. It was reported that some lattice oxygen ions in these catalysts have O^- character[1]. The O^- was the active species to form methyl radical from methane. It is expected that the lattice oxygen with O^- character is also present on the surface of Li^+-added Y_2O_3. However, in the XANES spectra of Li^+-added Y_2O_3, the peak due to O^- species could not be seen. This would be due to adsorption of CO_2 on Li^+-added Y_2O_3. During the oxidative cracking of n-butane at 1023 K, the O^- species may be formed on Li^+-added Y_2O_3 catalyst. In order to investigate the presence of the O^- species, *in situ* measurements should be needed.

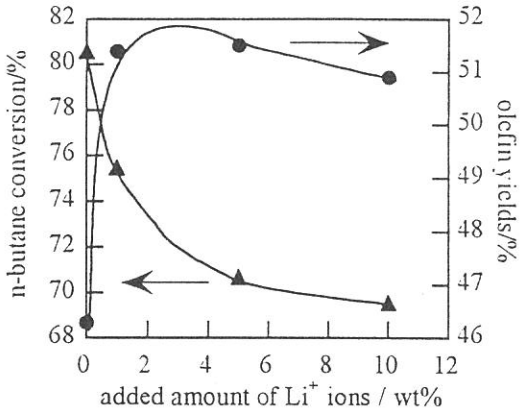

Fig.1 Change in n-butane conversion and olefin yield by added amounts of Li^+ ions.

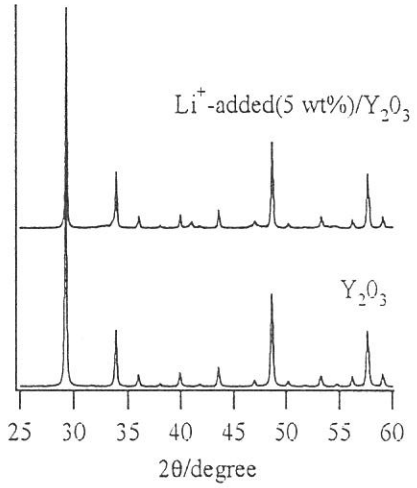

Fig. 2 XRD patterns of Y_2O_3 and Li^+(5 wt%)/Y_2O_3.

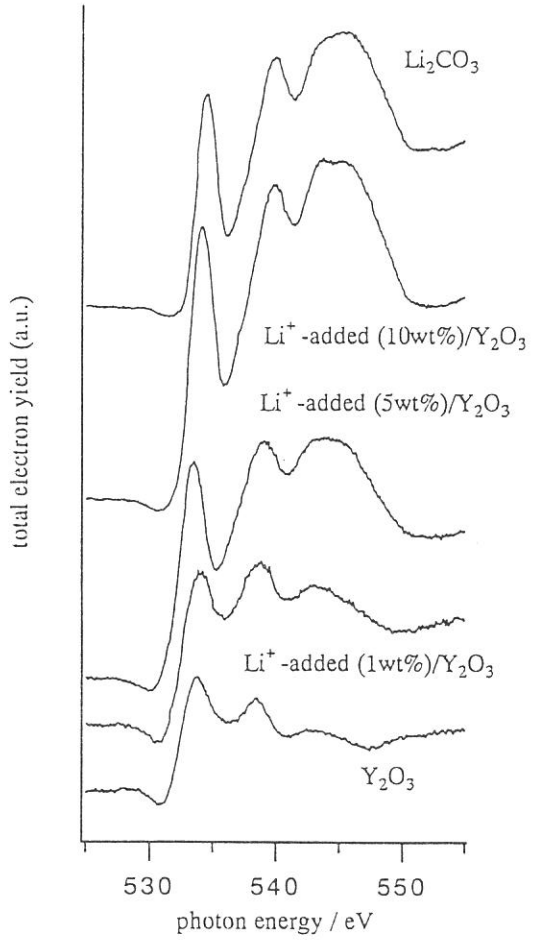

Fig. 3 O K-edge XANES spectra of Li^+-added Y_2O_3 catalysts and reference samples.

1) T. Ito and J. H. Lunsford, *Nature*, 314, 721 (1985)

(BL8B1)

Study on Photodissociation of Core-excited CH_3CN and CD_3CN by Using a Reflectron-type Time-of-flight Mass Analyzer

Yasunori Senba, Hiroaki Yoshida, Tetsuro Ogata, Daisuke Sakata, Atsunari Hiraya and Kenichiro Tanaka

Department of Physical Sciences, Hiroshima University, Higashi-Hiroshima 739-8526, Japan

The angular dependent mass spectra of fragment ions for gas phase acetonitrile (CH_3CN) and acetonitrile-d_3 (CD_3CN) following nitrogen core excitation were measured at beamline BL8B1 [1]. The variable-angle reflectron-type time-of-flight mass analyzer named "VARTMAN" [2] was used as an experimental apparatus. Briefly, this apparatus is equipped with a reflectron-type time-of-flight mass spectrometer (RTOF-MS) which has higher mass resolution than the conventional linear-type TOF-MS. Also the detection axis of the RTOF-MS is variable from –20 to +110 degrees with respect to the electric vector of the linearly polarized soft X-ray without breaking the vacuum. In the present measurements, the detection angle of the RTOF-MS was set perpendicular or parallel to the linear polarization axis (horizontal) of the soft X-ray beam.

TOF spectra were measured at the resonant excitation N1s to the π^*. In order to subtract the contribution of valence bands excitation, mass spectra were also measured below the core excitation threshold. Intensity of these spectra were normalized by photon intensity and accumulation time prior to the subtraction.

Figure 1 shows mass spectra obtained for the resonant excitation N1s→π^* of CH_3CN with perpendicular and parallel detection angle. In addition to CHx^+ (x = 0~3), N^+ and C_2Hx^+ (x = 0~3) observed in these mass spectra, singly charged fragment ions H^+, H_2^+, $HxCN^+$ (x = 0~2) and $CHxCN^+$ (x = 0~3) were observed. Only one doubly charged fragment ion CH_2CN^{2+} was also observed. In these spectra, characteristic triad features are observed at mass number 13, 14, 15, 25, 26 and 27, while single peaks are observed at each mass number 12, 24 and 28. The triad features are due to a difference in the initial kinetic energy (KE) of ions released in dissociation process, and consist of a sharp central peak (KE~0) and two broad wings (KE>0). The central peak and the wings correspond to different dissociation processes. In brief, ions (KE>0) ejected in the direction towards RTOF-MS are arrive at the micro sphere plate in shorter time-of-flight than ions with almost zero kinetic energy, while ions with kinetic energy ejected in the opposite direction arrive in longer time-of-flight. Hence, we can estimate the initial kinetic energy of ions from flight time difference between the wings and the central peak. The initial kinetic energy of fragment ions at the maximum distribution observed for N1s→π^* are summarized in Table 1. The total kinetic energy release for each process in Table 1 was estimated to be about 4~6 eV by assuming the two-body dissociation process.

In the fragmentations with mass number 14, 15, 26 and 27, significant difference in the intensity ratio of wings to the central peak is observed between the mass spectra obtained with parallel and perpendicular detection angles. These differences are ascribed to the angular distributions of the fragment ions. The isotropically dissociated ions form the wings at both detection angles, while the anisotropically dissociated ions form the wings at only one detection angle. These two different types of wings are termed as isotropic and anisotropic wings, respectively. For instance, the wings at mass number 14 obtained with a perpendicular detection angle consisted of the isotropic and anisotropic wings. The contribution of the anisotropic wings to the whole wings was estimated to be 55 % from the integrated intensity of the wings obtained with perpendicular and with parallel detection angle. The orientation of molecules in space was defined by the electric vector of monochromatic light and the transition moment when molecules were excited. Thus the anisotropic wings indicate that fragment ions have "memory" of molecular orientation, since dissociation occurs more rapidly than molecular rotation.

Two ion species, CH_2^+ and N^+, correspond to mass number 14 (See Table 1). In order to estimate the contribution of each ion species, the mass spectra for CD_3CN was also measured. Figure 2 shows the comparison of mass spectra obtained for CH_3CN and CD_3CN. The mass number 14 observed for CH_3CN is formed by CH_2^+ and N^+, and indicates the larger ratio of wings to central peak than that of CD_2^+ observed for CD_3CN. The mass number 14 observed for CD_3CN is formed by CD^+ and N^+, and indicates the larger ratio of wings to central peak than that of CH^+ observed for CH_3CN. Assuming that the branching ratio of mass species for CH_3CN and CD_3CN are the same, the N^+ form the majority of the wings at mass number 14. The contribution of the N^+ to the wings was estimated to be 60 % from the integrated intensity of the wings at mass number 14 (CH_2^+, N^+) for CH_3CN and at mass number 16 (CD_2^+) for CD_3CN. This ratio is almost the same as the ratio between the anisotropic and the isotropic wings at mass number 14 for CH_3CN described above. Thus we concluded that the wings at mass number 14 consist of isotropic and anisotropic wings, and the latter is formed only by the N^+ contribution. The similar anisotropic wings were found at mass number 15 (CH_3^+), 26 (CN^+) and 27 ($C_2H_3^+$). The fragment ions of mass number 14 and 27, 15 and 26 are considered as counterpart ion pairs for the C≡N, C–C bond cleavage, respectively. This is also supported by the fact that the observed kinetic energies of counterpart ions are consistently explained by two-body dissociation. From these points of view, it is concluded that the cleavage of the C–C or C≡N bond following N1s→π* takes place faster than the molecular rotation period.

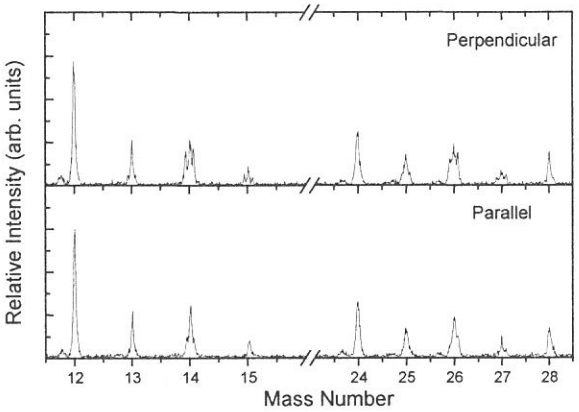

Figure 1. The mass spectra of acetonitrile (CH_3CN) following N1s→π* measured by perpendicular (top) and by parallel (bottom) detection axes.

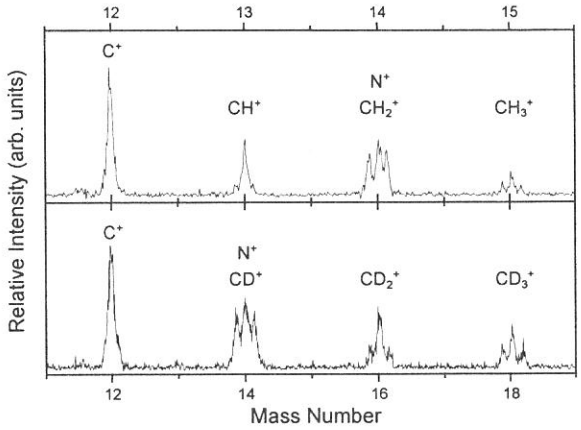

Figure 2. The mass spectra obtained for N1s→π* of CH_3CN (top) and CD_3CN (bottom).

References

[1] Y. Senba et al., J. Electron Spectrosc. Relat. Phenom. (1999), in press.

[2] A. Hiraya et al., J. Electron Spectrosc. Relat. Phenom. (1999), in press.

Table 1. The calculated initial kinetic energy of fragment ions observed for N1s→π* and the total kinetic energy release calculated by assuming the two-body dissociation process.

Mass number (Ion species)	Observed kinetic energy (eV)	Process of reaction	Kinetic energy release (eV)
13 (CH^+)	3.1 ± 0.4	$CH_3CN \rightarrow CH^+ + H_2CN$	4.5 ± 0.6
14 (CH_2^+)	2.6 ± 0.2	$CH_3CN \rightarrow CH_2^+ + HCN$	4.0 ± 0.3
14 (N^+)	4.3 ± 0.4	$CH_3CN \rightarrow N^+ + C_2H_3$	6.5 ± 0.6
15 (CH_3^+)	2.5 ± 0.2	$CH_3CN \rightarrow CH_3^+ + CN$	3.9 ± 0.3
26 (CN^+)	1.2 ± 0.1	$CH_3CN \rightarrow CN^+ + CH_3$	3.3 ± 0.3
27 ($C_2H_3^+$)	1.8 ± 0.1	$CH_3CN \rightarrow C_2H_3^+ + N$	5.3 ± 0.3
27 (HCN^+)	1.2 ± 0.1	$CH_3CN \rightarrow HCN^+ + CH_2$	3.5 ± 0.3

(BL8B1)

Faraday Rotation Measurement around Ni $M_{2,3}$ Edges Using Al/YB_6 Multilayer Polarizers

Tadashi Hatano, Weibing Hu, Katsuhiko Saito and Makoto Watanabe

Research Institute for Scientific Measurements, Tohoku University
2-1-1 Katahira, Aobaku, Sendai 980-8577

Magnetic circular dichroism (MCD) measurements in core absorption regions have been carried out explosively to investigate local magnetic states in ferro- and ferri-magnetic, alloy and multilayer systems, using circular polarization of synchrotron radiation. For easier sample preparation, the total photoelectron yield (TY) method with bulky samples or evaporated samples on thick substrates is usually employed [1] instead of the transmittance method with thin film samples [2]. However, the best performance of MCD measurements can not be brought out by the TY method in the studies of bulk materials or buried layers in multilayers, because the probing depth of the TY method is considered to be a few ten angstroms so that the obtained spectra are affected more or less with surface conditions. Furthermore, MCD measurements even including the transmission method would involve the ambiguity of the degree of circular polarization of incident monochromatized light, unless it were evaluated with an ellipsometric monitoring throughout the relevant energy range. The alternative approach to magneto-optical effects can be made by means of the Faraday rotation measurement. One can obtain the imaginary part of off-diagonal element of the dielectric tensor of the magnetized material by detecting the change of the azimuth of polarization ellipse between incident and transmitted lights (in principle, one can also obtain the real part by detecting the change of the ellipticity). In the core absorption regions, Faraday rotation measurements have been only performed by Kortright's group so far [3]. In our previous paper, we reported multilayer polarizers for use in the 55–90 eV region for Faraday rotation experiments around $M_{2,3}$ edges of 3*d* transition metals [4]. In the present work, we constructed a polarimeter for Faraday rotation measurements, which consists of a multilayer polarizer, a multilayer analyzer and a magnetic circuit. Measurements were carried out on Ni film samples around the $M_{2,3}$ absorption edges, and the results were compared with the rotation angle obtained by Kramers-Krönig (K-K) transform of a measured MCD spectrum [1].

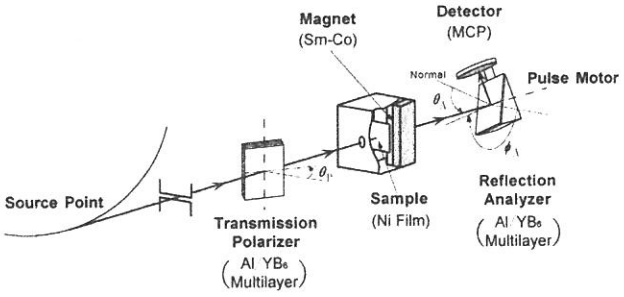

FIG. 1. Schematic illustration of the experiment at BL8B1.

The experiments have been performed at BL8B1. Schematic illustration is shown in fig. 1. Light incident to the sample was linearly polarized using the transmission polarizer between the post-focusing mirror and the sample chamber. The polarizer was a free-standing Al/YB_6 multilayer [4]. Three samples can be loaded on the sample holder at the same time. Samples are exchanged by linear motion of the sample holder. We will report the experimental results on four Ni samples in this paper. All samples were deposited on a collodion film supported with a copper mesh. The transmittance of the whole substrate (collodion and mesh) was about 35% in the spectral region of the present measurements. Samples #1 and #2 were made by magnetron sputtering to be 315 Å thick. Samples #3 and #4 were made by an evaporator of a BN composite boat and their thicknesses were 295 Å and 170 Å, respectively. Sample #4 was coated over in situ with a 330 Å thick aluminum by another evaporator to prevent surface pollution. Measurements were done at room temperature. The sample was magnetized in the Faraday configuration, in a magnetic field of 0.82 T generated by a magnetic circuit made of Sm-Co permanent magnet. The applied magnetic field of 0.82 T is stronger than the saturation magnetization of Ni (0.61 T at room temperature), though it is not obvious that the magnetization perpendicular to the film plane should be saturated. Rotation of polarization plane due to the magnetized sample was

detected by rotating analyzer ellipsometry [5,6]. The analyzer was an Al/YB_6 reflection multilayer fabricated simultaneously with the transmission polarizer. When the the azimuthal angle of the analyzer ϕ_A is rotated, the detector's output changes in the form of $1 + P_L \cos 2(\phi_A - \Phi_0)$, where P_L and Φ_0 are the degree of linear polarization and the azimuth of polarization ellipse, respectively.

We measured the degree of linear polarization P_L of the light out of the monochromator first, because P_L was expected to be lower than unity owing to non-ideal alignment of the beamline optics [6]. The transmission polarizer was set at normal incidence and thus measured P_L was 0.80 at 65 eV. By adjusting the angle of incidence of the polarizer (41.5° at 65 eV), P_L was improved to 0.98. The polarizance of the transmission polarizer was evaluated to be 0.8 from the fact that P_L increased from 0.80 to 0.98. Then we introduced the magnetized Ni samples in the optical path and measured the shift of the azimuth of polarization ellipse which corresponds to the Faraday rotation angle.

In fig. 2, measured Faraday rotation angles for samples #1, #2, #3 and #4 are plotted by closed circles, open circles, squares and triangles, respectively, against the photon energy. The sign of Faraday rotation angle is defined in regard to the direction of magnetic field. It seems that the rotation angles per sample thickness were constant, which implies that samples do not suffer surface pollution and reflect bulk properties well. The thick line in fig. 2 means Faraday rotation spectrum for the sample thickness of 315 Å obtained by K-K transform of the MCD spectrum [1]. The MCD spectrum had been measured at BL-28A, Photon Factory using a helical undulator of which peak photon energy was 70 eV. The sample temperature was 140K and the applied magnetic field was 1.05 T. The absorption was measured by the TY method in arbitrary unit and was re-scaled into the unit of absorption coefficient (cm^{-1}) according to the published optical constants [7]. In the numerical calculation of K-K transform, the energy integral was carried out with limits of 40 eV and 90 eV practically. Since magnetization of Ni sample at 140K is considered to be larger than that at room temperature, this calculated value should be larger than the present experimental value. As seen in comparison of the calculated rotation angle with the measured ones, #1 and #2, however, the absolute value obtained by K-K analysis was almost the same as or smaller than those of the present measurement. Therefore it was found that the previous MCD experiment [1] has given smaller value than that of intrinsic one. At present, it is not clear that this is due to the surface pollution or the insufficiency of the degree of circular polarization. Anyway, the careful estimation of the degree of circular polarization of incident light [8] have been necessary in the MCD measurements. Our experiment shows that absolute values of measured MCD data can be easily corrected by Faraday rotation measurements.

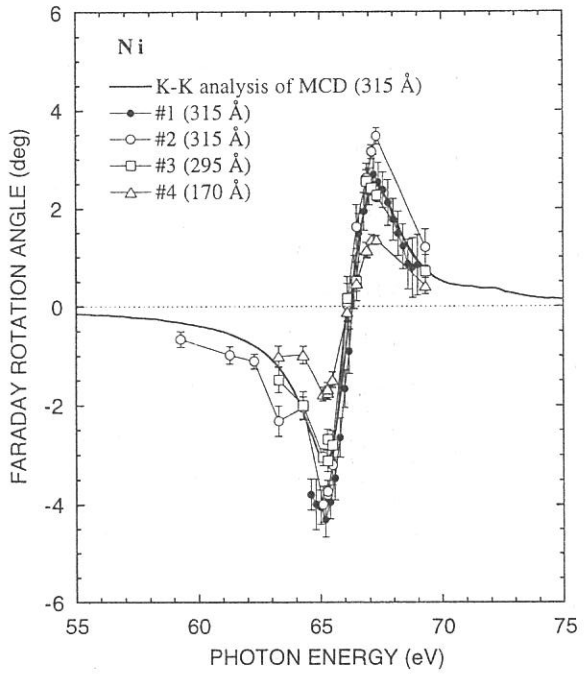

FIG. 2. Spectra of Faraday rotation angle measured at the present experiments and obtained by Kramers-Krönig transform of an MCD spectrum [1].

References

[1] T. Hatano, S. Y. Park, T. Hanyu and T. Miyahara, J. Electron Spectrosc. Relat. Phenom. **78**, 217 (1996).

[2] S. Muto, Y. Kagoshima and T. Miyahara, Rev. Sci. Instrum. **63**, 1470 (1992).

[3] J. B. Kortright, M. Rice and R. Carr, Phys. Rev. B **51**, 10240 (1995).

[4] W. Hu, T. Hatano, M. Yamamoto and M. Watanabe, J. Synch. Rad. **5**, 732 (1998).

[5] T. Hatano, W. Hu, M. Yamamoto and M. Watanabe, J. Electron Spectrosc. Relat. Phenom. **92**, 311 (1998).

[6] T. Hatano, W. Hu, M. Yamamoto and M. Watanabe, UVSOR Activity Report 1997, 64 (1998).

[7] E. D. Palik (Ed.), Handbook of Optical Constants of Solids, Academic Press Inc., 1985.

[8] T. Koide, T. Shidara, T. Miyahara and M. Yuri, Rev. Sci. Instrum. **66**, 1923 (1995).

(BL8B1)

Polarization-Dependent Nitrogen *K*-edge Absorption of InGaN

Kazutoshi FUKUI, Ryousuke HIRAI and Akio YAMAMOTO
Faculty of Engineering, Fukui University, Fukui 910-8507, Japan
Fax +81-776-27-8749, fukui@fuee.fukui-u.ac.jp

The soft X-ray absorption (SXA) around nitrogen *K*-edge have been measured to investigate the electronic structure of the wurzite III – V nitrides, especially the structure of the unoccupied states. The N *K* absorption spectra of III – V nitrides near the N *K*-edge in principle represent the partial density of the final states with *p* symmetry according to the selection rule. Since the core levels are strictly localized in space, the N *K* absorption spectrum gives us the site-specific information. The N *K* absorption spectrum also gives us the information about the final states symmetry p_{xy} and p_z, because the incidence soft X-ray light is linearly polarized.

The experiments were carried out at BL8B1. Resolution power under the experimental conditions were about 0.5 eV at 400 eV. The soft X-ray absorption measurement was performed by using the total photoelectron yield (TY) method. Thin films were made by the MOCVD method at RIKEN on SiC substrates, at Fukui University on GaAs(111) surface and at Nichia Chemical on α-Al_2O_3 substrate. All films were cleaned with organic solvents just before the installation in the vacuum chamber. No specific surface cleaning of the samples was performed in the vacuum chamber. The TY measurements were carried out at room temperature in the range of 10^{-9} Torr. Sample holder was able to rotate in the vacuum chamber for the angular dependent measurement. The incidence angle θ is defined as the angle between the incident light and the normal axis of the sample surface, i.e., c-axis. The incidence angle dependent SXA measurements were performed under the *p*-polarization configuration which means **E** parallel to *c*-axis at $\theta \sim 90°$, where **E** was the electric field of the incident light.

Figure 1 shows the N *K* absorption spectra of $In_{1-x}Ga_xN$. The energy scale is relative to the threshold energy which corresponds to the conduction band minimum. The labels A to G are corresponding to those for GaN in Ref. 1. The intensity of each spectrum is normalized at the peak B. The spectra features of GaN and InN are good agreement with the

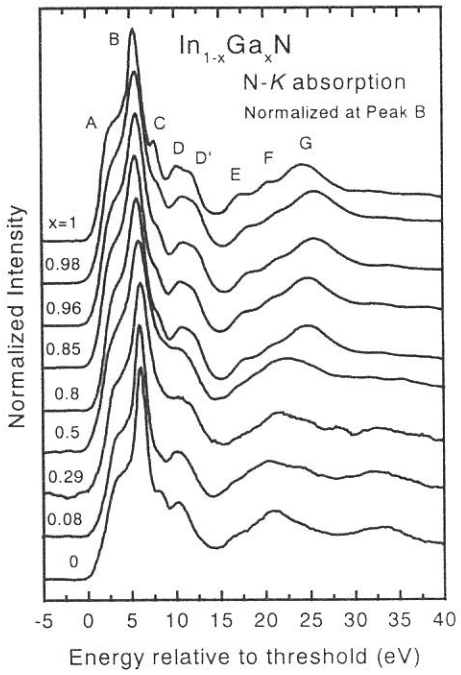

Fig.1 N K absorption spectra of InGaN. The energy scale is relative to the threshold energy.

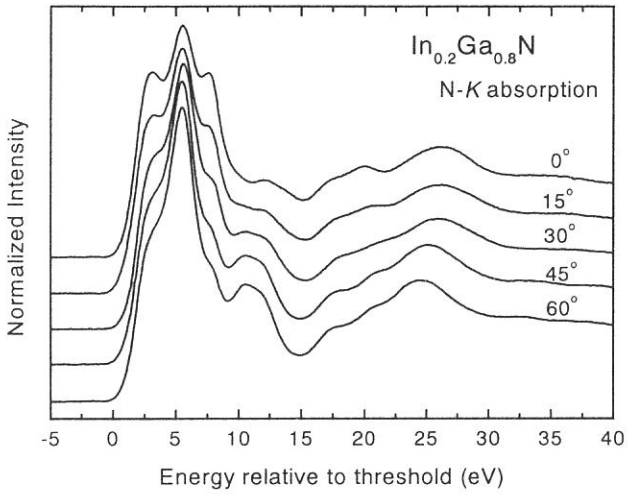

Fig. 2 N K absorption spectra of $In_{0.2}Ga_{0.8}N$ as function of angle which is defined as the angles between the incident light and the normal to the sample surface (c-axis).

previous works [1-3]. All spectra seem to be explained by the same labeling. It is suggested that the electric structures of the unoccupied states around nitrogen for III – V nitrides basically consist of the similar components. Figure 2 shows the N K absorption of $In_{0.2}Ga_{0.8}N$ as function of angle θ. All spectra are normalized at 34.5 eV. These types of angular dependence can be seen in all the samples. Each spectrum has angular dependent part and independent part, so that a numerical component analysis to separate the experimental spectrum into angular dependent and independent spectra has been performed under three assumptions as mentioned in Ref. 4. Figure 3 shows the partial spectra decomposed numerically from $In_{0.2}Ga_{0.8}N$ N K absorption spectra (Fig. 2). The three spectra labeled XY, Z and N correspond to p_{xy} , p_z, and angular independent components of the unoccupied p partial density of states around N-site, respectively. The spectrum labeled D represent the summation of the square residual error over whole spectra shown in Fig.2. The spectrum labeled M shows the calculated N K absorption spectrum at $\theta = 35.26^{\circ}$. In case of hexagonal sample, the spectrum at this angle (Magic angle) loses its anisotropic information which means that it is easy to compare experimental results with calculated partial density of states.

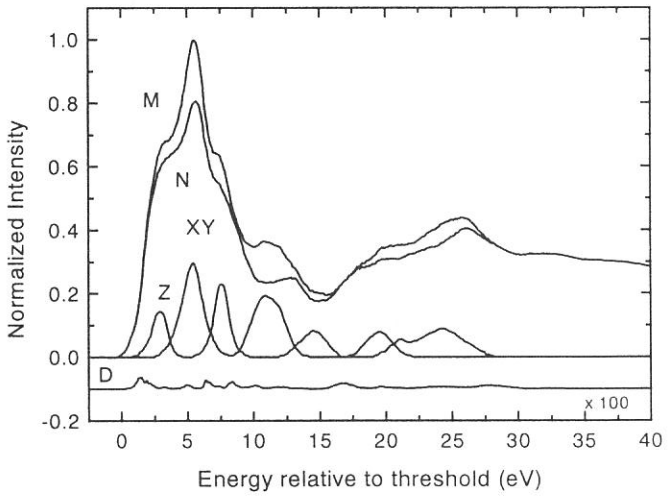

Fig. 3. Partial spectra decomposed numerically from N K absorption spectra of $In_{0.2}Ga_{0.8}N$. Three spectra labeled XY, Z and N correspond to in-plane, out-of-plane and angular independent components of the unoccupied p partial density of states at N-site, respectively. The spectra labeled M and D represent calculated K absorption spectrum at θ = 35.26° and the summation of the square residual error over whole spectra in Fig.2, respectively.

References

[1] W. R. L. Lambrecht, S. N. Rashkeev, B. Segall, K. Lawniczak-Jablonska, T. Suski, E. M. Gullikson, H. H. Underwood, R. C. C. Perera, J. C. Rife, I. Grzegory, S. Porowski and D. K. Wickenden, Phys. Rev. B **55** (1997) 2612.

[2] C. B. Stagarescu, L. -C. Duda, K. E. Smith, J. H. Guo, J. Nordgren, R. Singh and T. D. Moustakas, Phys. Rev. B **54** (1996) R17335.

[3] K. Fukui, M. Ichikawa, A. Yamamoto and M. Kamada, Solid State Electronics **41** (1997) 299.

[4] K. Fukui, R. Hirai and A. Yamamoto, UVSOR Activity Report 1997, 1998 p.184

(BL-8B1)

Measurement of Quantum Efficiency of the CCD Camera System

Atsuhiko Hirai[1], Kuniko Takemoto[2], Yasuyuki Nakayama[1] and Hiroshi Kihara[2]

[1] *Department of Physics, Ritsumeikan University, Kusatsu, Shiga 525-8577*
[2] *Physics Laboratory, Kansai Medical University, Hirakata 573-1136*

It has been realized that thinned back-illuminated CCD cameras without anti-reflective coatings are suitable as a detector of x-ray microscopy at water wavelength region [1, 2]. Since 1996, we have also been using a back-illuminated CCD (SiTe Ltd., SI502A) in our x-ray microscopy station [3], of which performance was measured as well as another type of CCD (EEV Ltd.) last year at UVSOR [4]. Contrary to our expectation, two CCD's show big difference in their quantum efficiency; the CCD of EEV showed quantum efficiency more than 20% from 1 to 10nm, whereas the other CCD of SiTe showed strong dependence on the wavelength and the quantum efficiency was less than 10% above 2nm. It was ascribed to the anti-reflective coating which should not be but was put accidentally. We, then, exchanged the CCD of SiTe to the new one without anti-reflective coating, and repeated the measurement of quantum efficiency of the SiTe CCD.

The CCD camera system consists of a CCD chip without the anti-reflective coating (SiTe Ltd., SI502-NAR), Astrocam CCD camera 4200 (liquid nitrogen cooling) and personal computer for camera controlling and data acquisition. The measurement system and the calculation system were basically the same with the last experiment with several improvements described below [4]. The scheme of the experimental arrangement is shown in Fig. 1. It consists of an aperture (6mm $\times$18mm), an Al attenuater (thickness, 2μm), a silicon photodiode (IRD AXUV-100) and the CCD camera system. In order to improve accuracy of the measurement, the number of incident photons were limited with the aperture and the attenuater. In the previous experiment, the absolute number of photons was measured by a drain current of an Au mesh, and was calibrated by the silicon diode (number of photons are counted by $n = h \cdot v/3.67$ eV) [4]. However, the drain current was a little too small to be measured with good accuracy. In the present experiment, then, the absolute number of photons was measured by the silicon diode directly. The number of detected photoelectrons was estimated from the CCD image [4].

The quantum efficiency of the CCD camera system thus estimated is shown in Fig. 2. The quantum efficiency decreases gradually with the increase of the wavelength. In water window region, the quantum efficiency shows a little higher than 20%. This result shows a quite similar tendency to the quantum efficiency of CCD (EEV Ltd.) [4].

There have been reports with quite different results. Aritome and his coworkers reported the quantum efficiency of CCD (EEV Ltd.) was c.a. 10% in water window region [5]; Wilhelm et al.

reported the quantum efficiency of CCD (SiTe Ltd.) was c.a. 55% in water window region [6]. It is not certain why the quantum efficiency are so different among the reports, but at least we can say the quantum efficiency of CCD would not depend on the fabrication company so much, as our measurements on CCD's of SiTe and EEV show similar results.

Acknowledgment

The authors are grateful for the help and encouragements from Prof. T. Kinoshita, Dr. T. Gejoh and other staffs of the Institute for Molecular Science.

References

[1] B. Niemann et al., X-ray Microscopy IV, eds. A. G. Michette et al. (Springer-Verlag, Berlin), 66 (1995).
[2] W. Meyer-Ilse et al., Synch. Rad. News 8, No.3 29 (1995).
[3] A. Hirai et al., UVSOR Activity Report 1995, 230 (1996).
[4] A. Hirai et al., UVSOR Activity Report 1996, 240 (1997).
[5] H. Aritome et al., SPIE 1741, 276 (1992).
[6] T. Wilhein et al., X-ray Microscopy IV, eds. A. G. Michette et al. (Springer-Verlag, Berlin), 470 (1995).

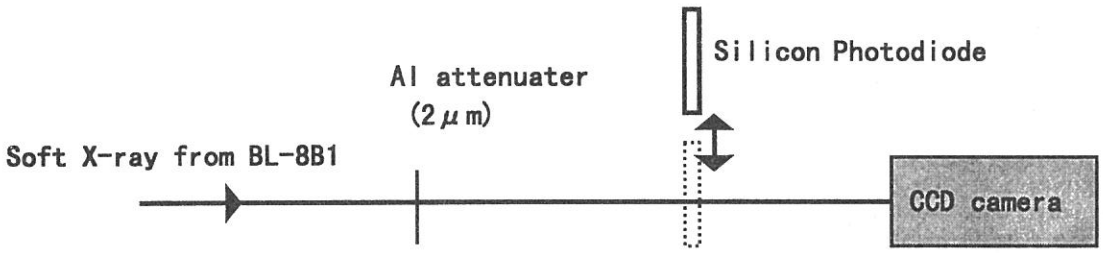

Fig. 1. Experimental setup arrangement.

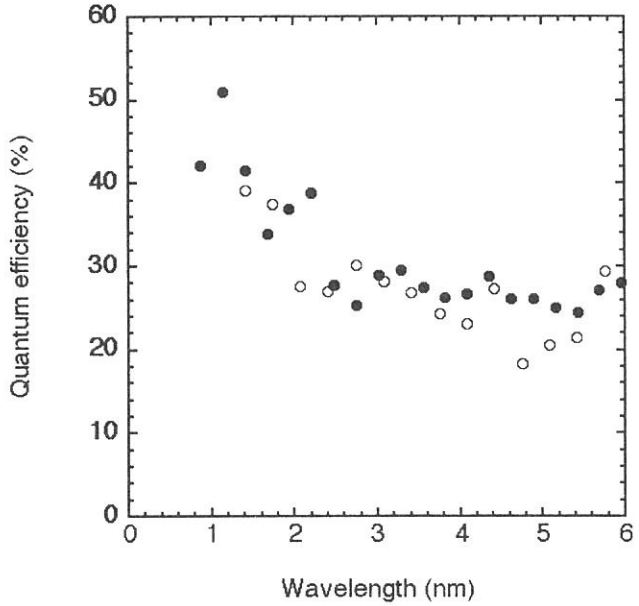

Fig. 2. Quantum efficiency of CCD camera system. ● is SITe CCD, and ○ is EEV CCD [4].

(BL8B1)

Oxidation States in $LiMn_2O_4$ Spinel Oxides from Transition Metal *L*-edge Spectroscopy

Yoshiharu UCHIMOTO, Takeshi YAO, Dan ISHIZAKI, and Taiji SASADA
Department of Fundamental Energy Science,
Graduate School of Energy Science, Kyoto University,
Yoshida, Sakyo-ku, Kyoto 606-8501, JAPAN

$LiMn_2O_4$ based spinel type oxides are one of the most promising cathode materials used in lithium ion batteries because their low cost, high theoretical energy density. In order to improve their cycle performance, several research groups have investigated the properties of manganese-substituted spinels of $LiM_yMn_{2-y}O_4$ (M=Cr, Ni, Co, etc.). These spinels show a decreased capacity on the 4.1 V plateau, however improved cycle life was reported for Co, Ni, and Cr doped spinels. Furthermore, recently Co, Ni, Cr, and Cu doped spinels show reversible redox processes at potentials above 4.5 V. (1, 2) It is important to clarify the structural change, valency change during charge and discharge process in order to understand their electrochemical properties. In the present study, transition metal doped spinels ($LiNi_yMn_{2-y}O_4$) were prepared. X-ray diffraction (XRD), X-ray Absorption Fine Structure (XAFS), and electrochemical studies were carried out. Especially, oxidation state of the transition metals in the $LiM_yMn_{2-y}O_4$ spinels were determined by using a measurement of Mn L_{23}-edge, Ni L_{23}-edge, and Oxygen *K*-edge X-ray Absorption Near Edge Structure (XANES). The Rietveld calculation was performed on the vector processor (Cray Y-MP2E/264) at the Institute for Chemical Research, Kyoto University, by using 'Rievec' computer program (3.4)

$LiNi_yMn_{2-y}O_4$ spinels were prepared from $LiNO_3$, $Mn(NO_3)_2$-$6H_2O$, $Ni(NO_3)_2$-$6H_2O$. The crystal structure of the product was determined by XRD using CuKα radiation. XRD pattern of $LiNi_{0.4}Mn_{1.6}O_4$ was indexed to an cubic lattice. The lattice parameters and other structural parameters were refined by the Rietveld method. Fig. 1 shows the results of the Rietveld analysis. The observed pattern agreed well with the calculated pattern. The obtained lattice parameters are given in Table 1. R_{wp}, R_F, and R_B are small enough to guarantee the reliability, and it was confirmed that $LiNi_{0.4}Mn_{1.6}O_4$ belonging to cubic *Fd3m* space group.

Figure 2 shows a low rate discharge curve of $LiNi_{0.4}Mn_{1.6}O_4$. The $LiNi_{0.4}Mn_{1.6}O_4$ shows mainly 2 different plateau regions. Between capacity = 0 to -30 mAh g^{-1} (the first plateau), the discharge voltage was of 3.5 to 4.5 V and then the charging curve has a plateau of about 4.7 V. XANES analysis were performed to clarify the oxidation state of manganese and nickel for various x values in $Li_xNi_{0.4}Mn_{1.6}O_4$.

Fig. 3 shows the Mn *L*-edge XANES of $LiNi_{0.4}Mn_{1.6}O_4$ at various potentials together with

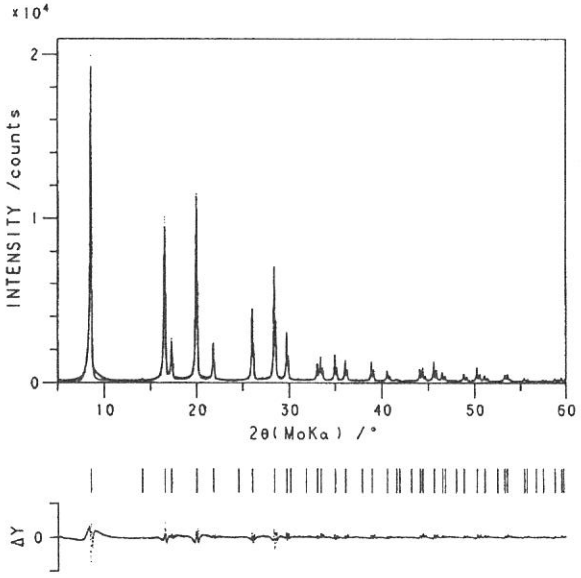

Fig.1 The observed (dot) and calculated (line) XRD patterns of $LiNi_{0.4}Mn_{1.6}O_4$. The difference between observed and calculated profiles is plotted below.

Table 1. Refined lattice parameters for $LiNi_{0.4}Mn_{1.6}O_4$

Cubic Spinel				
Space group : Fd3m				
Atom	site	x	y	z
Li	8a	0	0	0
Mn	16d	0.625	0.625	0.625
Ni	16d	0.625	0.625	0.625
O	32e	0.3875(1)	0.3875(1)	0.3875(1)
a = 8.17941(3) Å				
R_{wp},R_F,R_B = 0.0837,0.0344,0.0321				

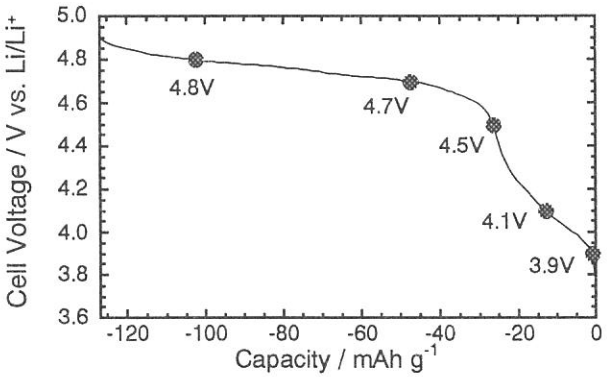

Fig. 2 Variations of electrode potential with capacity upon first charging of $LiNi_{0.4}Mn_{1.6}O_4$

MnO_2 (Mn^{4+}) and Mn_2O_3 (Mn^{3+}). The spectra correspond to $Mn2p^63d^n$ to $Mn2p^53d^{n+1}$ transitions. This figure shows that the Mn L_3 absorption edge of Mn_2O_3 was about 642.0 eV and that of MnO_2 was 643.4 eV. These results indicate that increasing the oxidation state of manganese, the Mn L_3 absorption edge shifted to higher energy. As shown in Fig. 3, the peak of $LiNi_{0.4}Mn_{1.6}O_4$ was a combination of peak of Mn_2O_3 and MnO_2. At low x value of $Li_xNi_{0.4}Mn_{1.6}O_4$ during the first plateau, contribution of Mn^{4+} increased. However, at the second plateau, the oxidation stage of Mn was 4+ and did not change.

Fig. 4 shows the Ni *L*-edge XANES of $LiNi_{0.4}Mn_{1.6}O_4$ at various potentials. The XANES spectra of $LiNi_{0.4}Mn_{1.6}O_4$ was in good agreement to that of NiO and did not change during the first plateau. At the second plateau, peaks at about 854.4 eV increased with increasing lithium deintercalation, however, the changes of the XANES spectra were very small. Fig. 6 shows O *K*-edge XANES of $Li_xNi_{0.4}Mn_{1.6}O_4$ at various potentials or x-values. The O *K*-edge

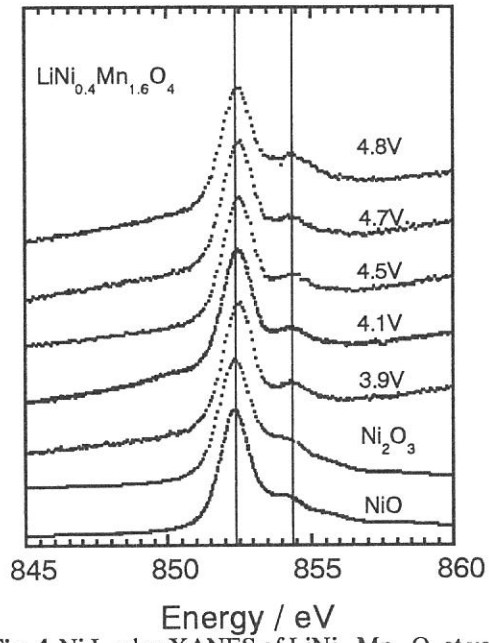

Fig. 4 Ni L-edge XANES of $LiNi_{0.4}Mn_{1.6}O_4$ at various potentials.

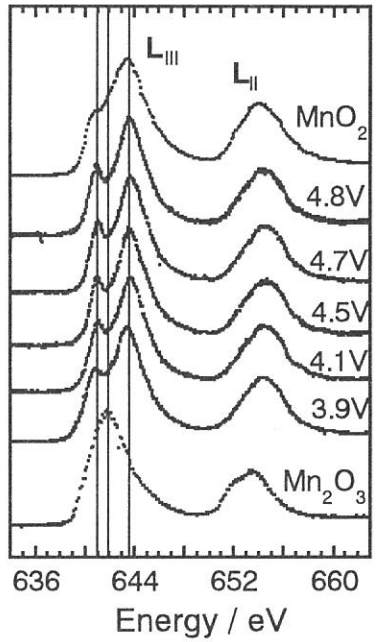

Fig. 3 Mn L-edge XANES of $LiNi_{0.4}Mn_{1.6}O_4$ at various potentials.

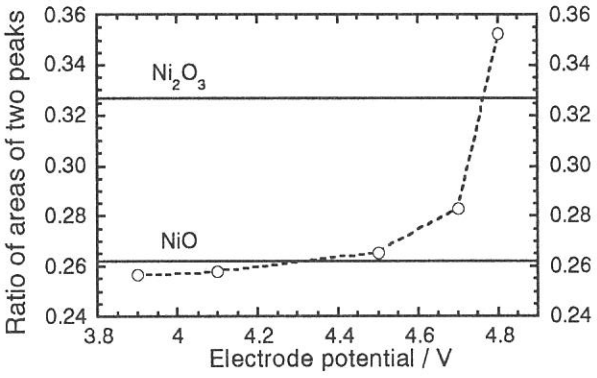

Fig. 5 Variations of peak ratio with electrode potential.

XANES spectra of $LiNi_{0.4}Mn_{1.6}O_4$ did not change during the first plateau. At the second plateau, peak increased with increasing lithium deintercalation. This results shows that oxidations found to take place on oxygen 2p orbital. These results show that $LiNi_{0.4}Mn_{1.6}O_4$ was a charge transfer insulator and that oxidations found to take place not on nickel but on oxygen 2p orbital mainly.

In conclusion, the average manganese valence in $LiNi_{0.4}Mn_{1.6}O_4$ was between 3 and 4 and the valence was increase during the electrochemical extraction of lithium at the first plateau. At the second plateau, manganese ions did not contribute to the oxidation reaction but the oxidations took place not on nickel but on oxygen 2p orbital mainly.

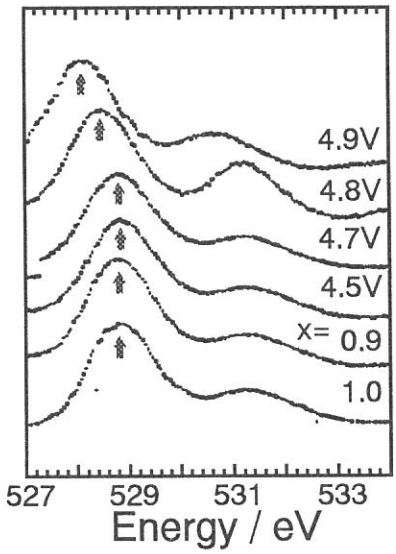

Fig. 6 O *K*-edge XANES of $Li_xNi_{0.4}Mn_{1.6}O_4$ at various potentials or x-values.

REFERENCES

1)Q. Zhong, A. Bonakdarpour, M. Zhang, Y. Gao, and J.R. Dahn, *J. Electrochem. Soc.*, **144**, 205 (1997).

2) Y. Todorov, C. Wang, and M. Yoshio, *Extended Abstract of 1997 ECS-ISE Joint Meeting*, **Vol. 97-2**, p. 94 (1997).

3) T. Yao, Y. Oka, and N. Yamamoto, *J. Mater. Chem.*, **32**, 331 (1992).

4) T. Yao, T. Ito, and T. Kokubo, *J. Materials Research*, **10**, 1079 (1995).

(BL8B1)

N and O *K* Shell Excitations of 5-Oxohexanenitrile

Toshio IBUKI
Kyoto University of Education, Fukakusa, Fushimi-ku, Kyoto 612-8522
Kazumasa OKADA and Ko SAITO
Department of Chemistry, University of Hiroshima, Higashi-Hiroshima 739-8526
Tatsuo GEJO
Institute for Molecular Science, Myodaiji, Okazaki 444-8585

It has been of great interest to control chemical bond fission of a free polyatomic molecule through a site selective core excitation followed by an Auger *KVV* process. In 1983 the C^+ and O^+ fragment ions were characteristically enhanced in the carbon *K* shell excited CH_3COCH_3.[1] However, little evidence has been provided for the site or state selectivity of a core excited free molecule. In this study we observed a typical site dependent photofragmentation occurring in the N and O *K* shell excitations of 5-oxohexanenitrile, $CH_3COCH_2CH_2CH_2CN$, in which five carbon atoms separate the interesting N and O atoms.

The experiments have been performed at the BL8B1 soft x-ray beamline. The energy scale was calibrated using the major soft x-ray peaks appeared in the total ion yield spectra of N_2 and O_2.[2] The total photoelectron-photoion coincidence spectra were acquired by using a reflectron type time-of-flight (R-TOF) mass spectrometer. The axis of the spectrometer was made at a magic angle with respect to the linearly polarized electric vector of the primary synchrotron radiation.

The total photoabsorption cross sections are shown in fig. 1a for the N and O *K* edge regions. The sharp peaks at 400.7 and 531.5 eV are assigned as the $\pi^*_{C\equiv N}\leftarrow$ N(1s) and $\pi^*_{C=O}\leftarrow$O(1s) excitations, respectively. The ionization potentials for $N(1s)^{-1}$ and $O(1s)^{-1}$ have not been reported so far as we know, and estimated to be ≈406 and ≈540 eV, respectively, from the analogs.

The R-TOF mass spectra are shown in figs. 1b and 1c for the $\pi^*_{C\equiv N}\leftarrow$N(1s) and $\pi^*_{C=O}\leftarrow$O(1s) excitations, respectively. The fragment ions larger than m/e=60 were negligible. The most abundant fragment ion is N^+ generated by the strongest C≡N bond fission at the N *K* shell excitation, while it is CH_3CO^+ at the O *K* edge. That is, the photofragmentation basically occurs at the strongly limited area excited initially as has been expected. The second strongest CO^+ fragment formation in the N *K* edge, however, suggests a unique Auger process would dominantly take place. The HOMOs of $\pi_{C\equiv N}$ of 5-oxohexanenitrile are followed by the closely lying $\pi_{C=O}$ molecular orbitals (MOs). Thus, the electrons lying in the $\pi_{C=O}$ and $\pi_{C\equiv N}$ MOs may be released as the Auger electrons to generate CO^+ and N^+

fragment ions. The Auger electron-photoion coincidence measurement is required to get more detailed information. It is noteworthy to point out that intramolecular H atom migration is very fast since the H_2O^+ molecular ion is observed in both the R-TOF mass spectra excited at the N and O *K* shell.

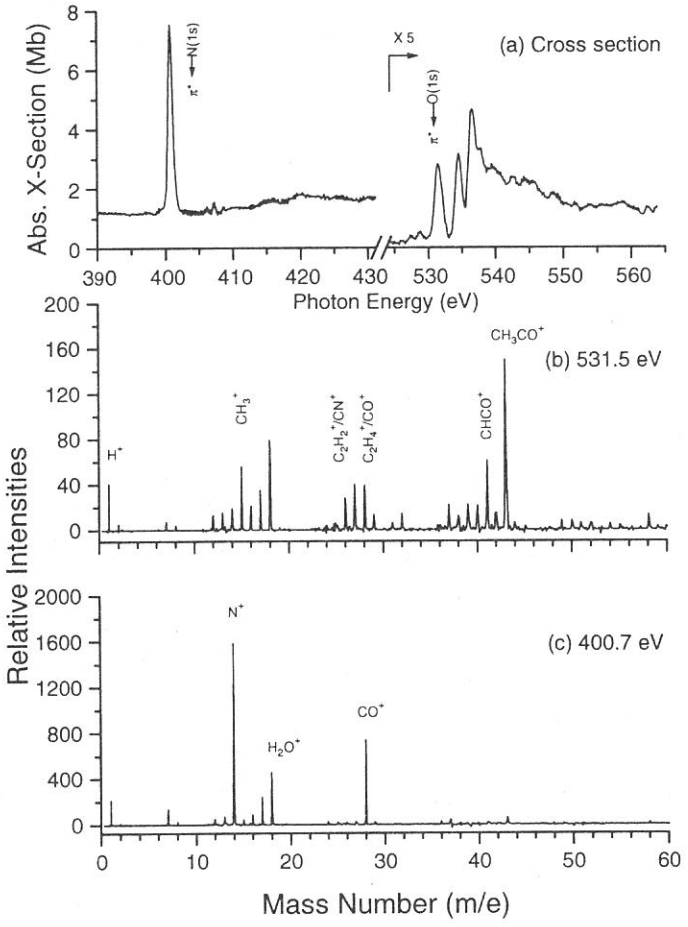

Fig. 1 Photoabsorption cross sections and R-TOF mass spectra at N and O *K* edges. (a) Photoabsorption cross section, (b) π*←O(1s), and (c) π*←N(1s).

References

1) W. Eberhardt, T. K. Sham, R. Carr, S. Krummacher, M. Strongin, S. L. Weng, and D. Wesner, Phys. Rev. Lett. **50**, 1038 (1983).
2) K. Lee, D. Y. Kim, C. I. Ma, D. A. Lapiano-Smith, and D. M. Hanson, J. Chem. Phys. **93**, 7936 (1990).